Computational homogenization of a physically-based crystal plasticity law for irradiated bainitic steels

Loïc Chaix, Mihail Gărăjeu, Martín Idiart, Ghiath Monnet, Pierre-Guy Vincent

Computational homogenization of a physically-based crystal plasticity law for irradiated bainitic steels

Loïc Chaix[a,b], Mihail Garajeu[a,*], Martín I. Idiart[c,d], Ghiath Monnet[e], Pierre-Guy Vincent[b]

[a] *Aix-Marseille Univ, CNRS, Centrale Marseille, LMA, 4 Impasse Nikola Tesla, CS 40006, 13453 Marseille Cedex 13, France.*

[b] *Institut de Radioprotection et de Sûreté Nucléaire (IRSN), PSN-RES/SEMIA/LSMA, B.P. 3, 13115 Saint-Paul-lez-Durance Cedex, France.*

[c] *Centro Tecnológico Aeroespacial/Departamento de Ingeniería Aeroespacial, Facultad de Ingeniería, Universidad Nacional de La Plata, Avda. 1 esq. 47 S/N, La Plata B1900TAG, Argentina.*

[d] *Consejo Nacional de Investigaciones Científicas y Técnicas (CONICET), CCT La Plata, Calle 8 N° 1467, La Plata B1904CMC, Argentina.*

[e] *EDF - R&D, MMC, Avenue des Renardières, Moret sur Loing, France.*

Abstract

The elasto-viscoplastic response of irradiated bainitic steels for pressure vessels of light water reactors is described by a multiscale micromechanical model. The model relies on a simplified set of complex constitutive equations describing intragranular flow under a wide range of temperatures, strain rates, and irradiation levels. These equations were themselves partially calibrated by multiscale analyses based on dislocation dynamics calculations, atomistic calculations, and experimental measurements. They include the contribution of jog drag, lattice friction, evolution of dislocation microstructures, and irradiation hardening. The scaling up of these intragranular laws to polycrystalline samples relies on a computational homogenization method which solves the field equations within periodic representative volume elements by means of Fast Fourier Transforms. This computational method proves advantageous relative to the finite element method in handling the complex microstructural morphology of the model required to achieve overall constitutive isotropy. Macroscopic simulations for uniaxial curves under different irradiation levels are first confronted to experimental curves to identify certain microscopic material parameters employed to describe the evolution of the mean-free path of dislocations with deformation. Subsequent comparisons for the evolution of the yield stress, irradiation hardening and the response to sudden strain-rate variations are then reported for a class of steels with various chemical compositions under wide ranges of temperature, loading rate and irradiation level. Good agreement is obtained in all cases. Finally, simulations are employed to explore the influence of the initial dislocation density on the intragranular stress and strain fields. An appreciable influence on the fields is observed during the elasto-viscoplastic transition but not deep in the plastic range.

Keywords: steels, neutron radiation, crystal plasticity, computational homogenization

1. Introduction

The mechanical integrity of pressure vessels is a critical issue in the long-term safety assessment of light water reactors. These vessels are made of bainitic steels which undergo progressive embrittlement with

*Corresponding author:

Email addresses: lchaix@lma.cnrs-mrs.fr (Loïc Chaix), mihai.garajeu@univ-amu.fr (Mihail Garajeu), martin.idiart@ing.unlp.edu.ar (Martín I. Idiart), ghiath.monnet@edf.fr (Ghiath Monnet), pierre-guy.vincent@irsn.fr (Pierre-Guy Vincent)

neutron radiation. Accounting for this embrittlement in advanced failure criteria requires knowledge of the entire elastoplastic response of the steels for a wide range of deformation rates, temperatures, and radiation doses [1]. Such a range of working conditions hampers the use of purely phenomenological descriptions of material behavior and calls for physically-based descriptions that explicitly account for the micromechanisms responsible for the behavior.

At the microscopic scale, bainitic steels exhibit a polycrystalline structure of a small grain size, mainly composed of ferritic laths packages and cementite inclusions [2, 3]. At smaller scales, a high density of dislocations, intragranular carbides and irradiation defects, such as solute clusters and dislocation loops, are observed [1]. Monnet et al. [4] have recently adapted the crystal plasticity law reported in [5] for pure iron to bainitic steels. The law accounts for multiple physical phenomena and follows from multi-scale analyses based on dislocation dynamics calculations, atomistic calculations, as well as on experimental observations. It considers two contributions to the intragranular plastic slip rate through a harmonic sum, each one depending on the resolved stress and on dislocation densities in a strongly nonlinear manner, and furthermore, involve critical resolved stresses which depend on the strain rate. Recent experience suggests that certain simplications to this crystal plasticity law, such as a reduction in the number of internal variables employed, can be introduced without appreciably altering its descriptive capabilities. The first purpose of this work is to put forward such simplified law, which is spelled out in Section 2. To assess their descriptive capabilities, crystal plasticity laws must be scaled up by some homogenization procedure. The second purpose of this work is to report on the suitability of a computational homogenization method based on the Fast Fourier Transform (FFT) to scale up crystal plasticity laws. The method has recently proved successful in scaling up a subclass of this crystal plasticity law wherein one of the two contributions to the plastic slip rate dominates [6]. From its inception [7], FFT methods have been widely used for computing the overall mechanical response of heterogeneous materials with complex microstructures, see [8] for a recent review. Compared to the finite elements method [9, 10], the advantage of using a FFT method generally lies in a more rapid computation and in a complexity reduction due to the absence of the mesh and the natural way to incorporate the periodicity conditions. Lebensohn [11] used for the first time the iterative scheme proposed by Moulinec and Suquet in the context of polycrystalline materials, followed by many other works, see [12] for a recent review about computational simulations of the mechanical behavior of polycrystalline materials. It was remarked that the classical FFT scheme is less accurate in the case of low rate-sensitivity materials or in the case of composite materials with high contrast between phases [13]. To overcome this limitation, but also in order to accelerate the convergence of the iterative method, different improved FFT formulations were proposed [13, 14, 15] and compared in [16]. In the present work, the basic scheme spelled out in Section 3 is employed. Homogenized models exhibiting overall constitutive isotropy follow from representative volume elements with the required microstructural complexity. A third purpose of this work is to confront model predictions with experimental measurements on a class of bainitic steels, and thus infer certain material parameters employed by the simplified crystal plasticity law to describe the evolution of intragranular mean-free path of dislocations during deformation. Comparisons for a wide range of scenarios are reported in Section 4. In addition, the homogenized model is employed to explore the influence of initial dislocation densities on the intragranular stress and strain fields. Finally, Section 5 closes the exposition with a summary of the main conclusions.

2. A simplified crystal plasticity law for irradiated bainitic steels

Central to the multiscale model developed in this work is a simplified version of the physically-based crystal plasticity law of [4] for bainitic steels. Compared to the original version, it involves fewer equations and simpler expressions, and therefore eases numerical implementations. In the following, the upper indexes (s) refer to the slip system number, while the lower indexes refer to the nature of the variable.

The crystal law assumes an additive decomposition of the infinitesimal strain into elastic and viscoplastic parts such that

$$\dot{\boldsymbol{\varepsilon}} = \mathbb{C}^{-1} : \dot{\boldsymbol{\sigma}} + \sum_{s=1}^{N} \dot{\gamma}^{(s)} \boldsymbol{\mu}^{(s)}, \tag{1}$$

or equivalently

$$\dot{\boldsymbol{\sigma}} = \mathbb{C} : \left(\dot{\boldsymbol{\varepsilon}} - \sum_{s=1}^{N} \dot{\gamma}^{(s)} \boldsymbol{\mu}^{(s)} \right), \tag{2}$$

where the symbol ":" represents the doubly contracted tensor product, $\boldsymbol{\varepsilon}$ and $\boldsymbol{\sigma}$ are the total strain and Cauchy stress tensors, respectively, while $\dot{\gamma}^{(s)}$ and $\boldsymbol{\mu}^{(s)}$ are the slip rate and Schmid tensor of system s. The elastic deformation is fully characterized by the stiffness tensor $\mathbb{C}$, which is assumed isotropic with shear modulus μ and Poisson's ratio ν. The viscoplastic deformation, in turn, is assumed to occur by slip along twelve slip systems ($N = 12$) belonging to the family $\langle 111 \rangle \{110\}$. In this connection, it should be remarked that the original crystal law [4] admitted slip over $\{112\}$ planes also. However, simulations suggested that the contribution of these additional slip planes to the overall deformation was not significant even for temperatures for which $\{112\}$ slip is theoretically likely to be activated.

2.1. Slip rates

The crystal law further assumes that each slip rate $\dot{\gamma}^{(s)}$ is the harmonic mean of a slip rate $\dot{\gamma}^{(s)}_{drag}$ controlled by jog-drag and a slip rate $\dot{\gamma}^{(s)}_{friction}$ controlled by lattice friction. In bainitic steels, two types of dynamic obstacles control the effective stress: the lattice friction at low temperature resulting from the non-planar core structure of screw dislocations and jog drag induced by the thermally activated motion of jogs formed by intersection of mobile screw dislocations with forest dislocations whose Burgers vector is outside the slip plane. The harmonic sum

$$\dot{\gamma}^{(s)} = \left(\frac{1}{\dot{\gamma}^{(s)}_{drag}} + \frac{1}{\dot{\gamma}^{(s)}_{friction}} \right)^{-1} \tag{3}$$

reflects the fact that the slip occurs according to the characteristic times of the two physical phenomena. Each slip rate is given by

$$\dot{\gamma}^{(s)}_{drag} = \dot{\gamma}_{0,drag} \quad \sinh\left(p_{drag} \frac{\tau^{(s)}_{eff}}{\tau^{(s)}_{c}} \right) \operatorname{sgn}\left(\tau^{(s)} \right) \tag{4}$$

and

$$\dot{\gamma}^{(s)}_{friction} = \dot{\gamma}_{0,friction} \quad \exp\left(-\frac{\Delta G_0}{kT} \right) \sinh\left(\frac{\Delta G_0}{kT} \sqrt{\frac{\tau^{(s)}_{eff}}{\tau_0}} \right) \operatorname{sgn}\left(\tau^{(s)} \right), \tag{5}$$

where k is the Boltzmann constant, T is the absolute temperature, $\tau^{(s)} = \boldsymbol{\sigma} : \boldsymbol{\mu}^{(s)}$ is the resolved shear stress, $\tau^{(s)}_{eff}$ is an effective shear stress defined below, and the remaining symbols refer to material parameters characterizing slip. At high temperatures or low rates the flow is controlled by (4), whereas at low temperatures or high rates the flow is controlled by (5). For both regimes, a hyperbolic sine function is introduced to account for the probability, at low stress, of thermal activation in the opposite direction. This is an important improvement of the original model, since it allows to avoid discontinuity of slip rate at zero effective stress.

Given the common microstructural features in all bainitic steels, only the term $\tau^{(s)}_{c}$ varies between specific steels and increase with deformation in expressions (4) and (5). In these two equations, $\tau^{(s)}_{eff}$ is the effective shear stress for each slip system, that is, the net driving force for dislocation motion

$$\tau^{(s)}_{eff} = \max\left(|\tau^{(s)}| - \tau^{(s)}_{c},\ 0 \right). \tag{6}$$

The shear stress for each slip system is split into the critical shear stress, $\tau^{(s)}_{c}$, representing the yield surface at the given strain rate, and the effective shear stress $\tau^{(s)}_{eff}$ necessary to force screw dislocations to move at the velocity required to accommodate the imposed strain rate.

2.2. Critical shear stresses

In bainitic steels, the flow stress is controlled by a low-alloy Fe-C solid solution, intragranular carbide particles, high density of dislocations, small grain size (large Hall-Petch effet) and, if irradiated, irradiation defects such as dislocations loops (DLs) and solute clusters (SCs). These features can be classified into two families: local obstacles (dislocations, carbides, SC, etc.) and diffuse (or long-range) obstacles inducing solid solution and the Hall-Petch effect. Since solid solution and carbide contributions to the flow stress are substantially lower than the Hall-Petch effect and forest hardening, respectively, we incorporate the contribution of solid solution into that of the Hall-Petch effect (through a slight decrease in grain size) and we incorporate the carbide contribution into that of forest dislocations (through a small increase in dislocation density). This is a second simplification of the original model [4]. Thus, the critical stress is reduced to

$$\tau_c^{(s)} = \sqrt{\left(\tau_{auto}^{(s)}\right)^2 + \left(\max\left(\tau_{forest}^{(s)} - \tau_{eff}^{(s)},\ 0\right)\right)^2 + \left(\tau_{DL}\right)^2 + \left(\tau_{SC}\right)^2} + \tau_{HP}, \tag{7}$$

where the components

$$\tau_{auto}^{(s)} = \mu b\sqrt{a^{(s)(s)}\rho^{(s)}} \qquad \text{and} \qquad \tau_{forest}^{(s)} = \mu b\sqrt{\sum_{s\neq j} a^{(s)(j)}\rho^{(j)}}$$

account for the interactions of the dislocations belonging to the same slip system and for interactions of the dislocations belonging to different slip systems, respectively, while the remaining components

$$\begin{aligned}
\tau_{DL} &= \mu b\sqrt{a_{DL}\ d_{DL}\, c_{DL}}, \\
\tau_{SC} &= \mu\sqrt{p_{SC,1}\ \left(d_{SC}\right)^{2.3}\ \left(c_{SC}\right)^{1.14}}, \qquad (d_{SC} \text{ in nm and } c_{SC} \text{ in } 10^{22}\times \mathrm{m}^{-3}), \\
\tau_{HP} &= \frac{\mu}{\mu_{300K}}\frac{K_{HP}}{\sqrt{d}},
\end{aligned}$$

do not depend on the internal variables —and hence on the mechanical process— and refer, respectively, to the resistance of dislocation loops, solute clusters, and finally the contribution of the Hall-Petch effect —including solid solution— which depends on the average ferrite lath package size d. The internal variables $\rho^{(s)}$ refer to the dislocation densities on each active slip system. The Hall-Petch effect is here only described by a mean grain size d. It has been shown that the sizes of the ferrite lath packages and old austenitic grains are proportional [17], which justify the choice of a single parameter to describe the microstructure. The added value of our work is to show that we can isolate the Hall-Petch effect and obtain a flow stress while respecting both the experimentally measured dislocation densities and the Hall-Petch law with an experimentally measured Hall-Petch constant, which was not a foregone conclusion. In turn, the volume densities of irradiation defects c_{DL} and c_{SC} and their sizes d_{DL} and d_{SC} are material parameters that can be predicted by microstructure models or measured in experiment. The interaction coefficients $a^{(s)(j)}$ are defined such that, taking into account the results of dislocation dynamics simulations and by making a first order approximation on the strength of the junctions, two different values are considered: 0.7 for the collinear interactions (system sharing the same Burgers vector) and 0.1 for all other configurations. The remaining symbols in these expressions are defined in Table 1, unless some parameter values which are obtained by comparison with experimental data and will be given further. As pointed out in [4], an important modification to the original model is that the contributions of DL and SC are now outside the max() term in expression (7). The reason was discussed in [4]. This modification is significant and must be taken into account.

2.3. Evolution of dislocation densities

Physically-based crystal plasticity laws include equations for the evolution of the internal variables describing the microstructure (dislocations, dislocations loops, solutes clusters, among others). It is assumed that only the dislocation density on each slip system can vary (dislocation loops and solute cluster densities

Symbol	Parameter	Value	Units
μ	shear modulus	$82819.0 - 8.17\ T(K)$ $-0.0213\ T^2(K)$	MPa
ν	Poisson ratio	0.3	–
$\dot{\gamma}_{0,drag}$	reference slip rate for the jog drag contribution	10^{-5}	s^{-1}
$\dot{\gamma}_{0,friction}$	reference slip rate for the lattice friction contribution	10^{9}	s^{-1}
p_{drag}	parameter adjusted from experimental results	200.0	–
ΔG_0	parameter adjusted from experimental results	0.84	eV
k	Boltzmann constant	8.6×10^{-5}	$eV.K^{-1}$
τ_0	reference critical shear stress	300.0	MPa
K_{HP}	constant related to the Hall-Petch effect	0.28	$MPa.m^{1/2}$
b	Burger vector norm	0.248	nm
a_{DL}	interaction coefficient for dislocation loops	0.25	–
$p_{SC,1}$	parameter related to the solute clusters	$0.3722 \times 10^{-12.38}$	$m^{1.12}$
p_d	parameter related to the ferrite lath package size	3.455	–
$p_{SC,2}$	parameter related to the solute clusters	4.0775×10^{11}	$m^{-5/4}$
T_0	characteristic temperature	217.4	K
$\rho_{init}^{(s)}$	initial dislocation density on each slip system	*	m^{-2}
d	average ferrite lath package size	*	μm
K_{auto}	number of obstacles (dislocation of the same system)	*	–
K_{forest}	number of obstacles (dislocation of a different system)	*	–
K_{DL}	number of obstacles (dislocation loops)	*	–
K_{SC}	number of obstacles (solute clusters)	*	–
p_y	parameter related to the annihilation distance	*	nm
d_{DL}	characteristic diameter of dislocation loops	*	nm
c_{DL}	concentration of dislocation loops	*	m^{-3}
d_{SC}	characteristic diameter of solute clusters	*	nm
c_{SC}	concentration of solute clusters	*	m^{-3}

Table 1: Material parameters of the crystal plasticity law. Numerical values correspond to steels resembling A508 cl.3 RPV available from the literature. Starred values are determined in this work.

remain fixed). According to the Kocks-Mecking classical theory [18], the storage of dislocations results from their immobilization after sliding over a distance λ, called mean free path. On the other hand, when the density increases sharply, spacing between dislocations decreases strongly. Below a critical spacing y (the annihilation distance), it is assumed that dipoles are no longer stable and annihilate spontaneously by thermal activation. The classical Kocks-Mecking formulation [18] can be written as

$$\dot{\rho}^{(s)} = \frac{|\dot{\gamma}^{(s)}|}{b} \left(\frac{1}{\lambda^{(s)}} - y\rho^{(s)} \right) \tag{8}$$

with the total mean free path of dislocations

$$\frac{1}{\lambda^{(s)}} = \frac{p_d}{d} + \frac{\sqrt{a^{(s)(s)}\rho^{(s)}}}{K_{auto}} + \frac{\sqrt{\sum_{s\neq j} a^{(s)(j)}\rho^{(j)}}}{K_{forest}} + \frac{\left(\frac{c_{SC}}{p_{SC,2}}\right)^{4/7}}{K_{SC}} + \frac{\sqrt{a_{DL}\ \ d_{DL}\ c_{DL}}}{K_{DL}}. \tag{9}$$

Each term in this last expression corresponds to a different class of obstacles to dislocation movement. The constants K_i represent the number of obstacles of the family i that can be overcome by a dislocation before its immobilization. In other words, equation (9) means that a dislocation is immobilized when it reaches a grain boundary and each time it encounters K_i obstacles of the family i. The values for the parameters K_i therefore influence hardening. A notable consequence of this approach is the presence of irradiation defects which modify the rate of the hardening in the irradiated materials. Due to thermal activation, the annihilation distance y depends on temperature according to

$$y = p_y\ \min(1,\ 0.255\ e^{T/T_0}). \tag{10}$$

The remaining material parameters entering expressions (2) to (10) are described in table 1. The numerical values reported in that table correspond to steels resembling A508 cl.3 RPV steels of interest in this work. The starred values will be chosen later for specific steels and determined from comparisons with experimental uniaxial curves.

3. Computational homogenization method

The macroscopic behavior of polycrystalline aggregates is characterized by the relation between the volume averages over the representative volume element of the local stress field, denoted $\bar{\boldsymbol{\sigma}}(t)$, and the local strain field, denoted $\bar{\boldsymbol{\varepsilon}}(t)$, where t is the time. To compute the stress and strain fields for a given loading condition, the constitutive equations presented in Section 2 are implemented in the computer code CraFT [19] which solves the mechanical field equations by means of a Fast Fourier Transform (FFT) based algorithm proposed in [20], [7], and [21] to determine the effective properties of periodic composites with complex microstructures. As in studies [22] and [23] devoted to the effective behavior of porous viscoplastic crystals and polycrystals, the so-called "basic" iterative scheme is adopted, which ensures the strain compatibility. At each time step CraFT determines the local stress and strain fields $(\boldsymbol{\sigma}, \boldsymbol{\varepsilon})$ by a fixed point algorithm

$$\begin{cases} \boldsymbol{\varepsilon}^{\mathrm{i}+1} = \boldsymbol{\varepsilon}^{\mathrm{i}} - \boldsymbol{\Gamma}^0 * \boldsymbol{\sigma}^i \\ \boldsymbol{\sigma}^{i+1} = \mathcal{F}(\boldsymbol{\varepsilon}^{i+1}, \boldsymbol{\varepsilon}^i, \boldsymbol{v}_{int}) \end{cases} \tag{11}$$

where at each iteration step i of the iterative scheme, the system of constitutive equations of the model, giving the function $\mathcal{F}$, is integrated in time using a fully implicit scheme ($\boldsymbol{v}_{int}$ corresponds to the internal variables). In (11) the operator $\boldsymbol{\Gamma}^0$ is the Green operator associated to an elasticity tensor $\mathbb{C}_0$ of an infinite medium ($*$ denotes the convolution operator). The choice of $\mathbb{C}_0$ can depend on the local constitutive behavior being simulated and plays an important role in the convergence rate of the algorithm. The present work relies on the choice already implemented in the code CraFT.

3.1. Convergence criteria

Since the "basic" scheme used in the computations presented in this work ensures the compatibility of the strain, only two convergence criteria are checked, one for the equilibrium condition and the other for the macroscopic stress direction (see Figure 1 of [24] for an intuitive representation of the convergence path). At each iteration i of the general algorithm in CraFT, the error relative to the local equilibrium condition is given by

$$\frac{\sqrt{\langle \|div(\boldsymbol{\sigma}^i)\|^2 \rangle}}{\|\langle \boldsymbol{\sigma}^i \rangle\|} \tag{12}$$

	Algorithm inputs: $\dot{\boldsymbol{\varepsilon}}^n$, $\boldsymbol{\sigma}^{n-1}$, $\dot{\gamma}^{n-1}$, τ_c^{n-1} and ρ^{n-1}
1	Initialization of the stress and the internal variables
	$\boldsymbol{\sigma}^{n,0} = \boldsymbol{\sigma}^{n-1}$, $\dot{\gamma}^{n,0} = \dot{\gamma}^{n-1}$, $\tau_c^{n,0} = \tau_c^{n-1}$ and $\rho^{n,0} = \rho^{n-1}$
2	Initialization of the error $\epsilon = tol + 1$
3	While $\epsilon > tol$
3.1	Calculation of $\boldsymbol{\sigma}^{n,i}$, $\dot{\gamma}^{n,i}$, $\tau_c^{n,i}$ and $\rho^{n,i}$
	$\boldsymbol{\sigma}^{n,i} = \boldsymbol{\sigma}^{n-1} + \Delta t\ f_1\left(\dot{\gamma}^{n,i-1},\ \dot{\boldsymbol{\varepsilon}}^n\right)$, f_1 corresponds to (2)
	$\dot{\gamma}^{n,i} = f_2\left(\tau_c^{n,i-1},\ \boldsymbol{\sigma}^{n,i-1}\right)$, f_2 corresponds to (3)
	$\tau_c^{n,i} = f_3\left(\tau_c^{n,i-1},\ \rho^{n,i-1},\ \boldsymbol{\sigma}^{n,i-1}\right)$, f_3 corresponds to (7)
	$\rho^{n,i} = \rho^{n-1} + \Delta t\ f_4\left(\rho^{n,i-1},\ \dot{\gamma}^{n,i-1}\right)$, f_4 corresponds to (8)
3.2	Calculation of the error
	$\epsilon_{\boldsymbol{\sigma}} = 2\left\|\boldsymbol{\sigma}^{n,i} - \boldsymbol{\sigma}^{n,i-1}\right\| / \left\|\boldsymbol{\sigma}^{n,i} + \boldsymbol{\sigma}^{n,i-1}\right\|$
	$\epsilon_{\dot{\gamma}} = 2\left\|\dot{\gamma}^{n,i} - \dot{\gamma}^{n,i-1}\right\| / \left\|\dot{\gamma}^{n,i} + \dot{\gamma}^{n,i-1}\right\|$
	$\epsilon_{\tau_c} = 2\left\|\boldsymbol{\tau}_c^{n,i} - \boldsymbol{\tau}_c^{n,i-1}\right\| / \left\|\boldsymbol{\tau}_c^{n,i} + \boldsymbol{\tau}_c^{n,i-1}\right\|$
	$\epsilon_{\rho} = 2\left\|\rho^{n,i} - \rho^{n,i-1}\right\| / \left\|\rho^{n,i} + \rho^{n,i-1}\right\|$
	$\epsilon = max\left(\epsilon_{\boldsymbol{\sigma}},\ \epsilon_{\dot{\gamma}},\ \epsilon_{\tau_c},\ \epsilon_{\rho}\right)$
3.3	Updating variables, affected by a weight $w \in [0,1]$ (in order to facilitate the convergence)
	$\boldsymbol{\sigma}^{n,i} = w\ \boldsymbol{\sigma}^{n,i-1} + (1-w)\ \boldsymbol{\sigma}^{n,i}$
	$\dot{\gamma}^{n,i} = w\ \dot{\gamma}^{n,i-1} + (1-w)\ \dot{\gamma}^{n,i}$
	$\tau_c^{n,i} = w\ \tau_c^{n,i-1} + (1-w)\ \tau_c^{n,i}$
	$\rho^{n,i} = w\ \rho^{n,i-1} + (1-w)\ \rho^{n,i}$
	Algorithm output: $\boldsymbol{\sigma}^n$

Table 2: Algorithm used for the numerical integration of the local crystal plasticity law in CraFT

where $\langle\boldsymbol{\sigma}^i\rangle$ denotes the volume average of the field $\boldsymbol{\sigma}^i$ and $\|\mathbf{.}\|$ denotes the Frobenius norms of a vector or a second-order tensor. This error is computed in the Fourier space. The error relative to the prescribed direction of the macroscopic stress is defined by

$$\frac{||\langle\boldsymbol{\sigma}^i\rangle - \boldsymbol{\Sigma}_0\ \ k^i||}{||\boldsymbol{\Sigma}_0\ \ k^i||}. \tag{13}$$

where $\boldsymbol{\Sigma}_0$ is the direction of the macroscopic stress and k^i indicates the level of macroscopic stress. In this work, the tolerances for both criteria are set to 10^{-3} (see also the general presentation of the two corresponding convergence tests in [25]).

3.2. Time integration of the local crystal plasticity law

The set of equations associated with the crystal plasticity law is highly nonlinear. A fully implicit scheme is chosen (implicit Euler scheme resolved by a fixed point algorithm) in order to determine the stress $\boldsymbol{\sigma}^{i+1}$ for a given strain $\boldsymbol{\varepsilon}^{i+1}$, at each CraFT iteration. The numerical procedure is presented in Table 2. In this

	C	S	P	Si	Cr	Mo	Mn	Ni	V	Al	Co	Cu
A	0.139	0.004	0.006	0.19	0.21	0.49	1.33	0.73	< 0.01	0.025	0.020	0.06
B	0.160	0.004	0.008	0.22	0.22	0.51	1.33	0.76	< 0.01	/	0.017	0.07
C	0.140	/	0.005	0.23	/	0.55	1.44	0.86	/	/	/	0.41
D	0.150	0.006	0.013	0.22	0.19	0.52	1.31	0.70	0.009	0.022	0.020	0.07

Table 3: Chemical composition in weight % of the various steels considered in this study

table, the index n and $n-1$ respectively refer to the current and previous times (Δt is the time step) and the index i and $i-1$ respectively refer to the current and previous iteration of the fixed point algorithm.

4. Results and discussion

The predictive capabilities of the homogenized model are assessed by confronting predictions with experimental uniaxial curves of four bainitic steels of a common class. Each steel is identified with letters A through D for ease of presentation; their chemical compositions are displayed in Table 3. Types A and D refer to a low copper steel and a 16MND5 steel, both resembling an A508 cl.3 steel. Type B refers to a 16MND5 steel employed in vessels for pressurized water reactors and manufactured by Framatome; it was subject to two austenitizing treatments followed by water quenching and tempering, and a final stress relief treatment to obtain a tempered bainitic microstructure. Finally, type C refers to RPV steel. For these steels, it is reasonable to assume that the influence of dislocation loops is negligible compared to that of solute clusters. Therefore, we set $c_{DL} = 0$ henceforth, and ignore the irrelevant parameters K_{DL} and d_{DL}. The reminder of the unquantified material parameters of Table 1 are identified by comparisons of predictions with experiments. To that end, uniaxial curves are simulated by applying mixed loading conditions of the form

$$\overline{\boldsymbol{\sigma}}(t) = k(t)\boldsymbol{\Sigma}_0 \qquad \text{and} \qquad \boldsymbol{\Sigma}_{\mathbf{0}} : \dot{\overline{\boldsymbol{\varepsilon}}} = \dot{E}, \tag{14}$$

where $k(t)$ is an unknown scalar function, evolving in time, $\overline{\boldsymbol{\varepsilon}}$ and $\overline{\boldsymbol{\sigma}}$ are the macroscopic strain and stress, $E(t) = \dot{E}\, t$ is the prescribed projected macroscopic strain in the $\boldsymbol{\Sigma}_0$ direction. We begin by identifying a suitable microstructural morphology for the computational model such that the simulated uniaxial curve produced by (14) is insensitive to loading direction $\boldsymbol{\Sigma}_0$. In the following, the tolerance *tol* is set to 10^{-4} and the weight w is set to 0.9.

4.1. Microstructural morphology

The microstructural morphology of bainitic steels is idealized as a periodic aggregate of grains defining a Voronoi tessellation. Note that the FFT method can also be used to perform computations on other types of tessellations, such as those of Johnson-Mehl-Avrami-Kolmogorov and Laguerre, see [26]. A Voronoi tessellation is generated from random grain seeds using a minimal distance algorithm. Crystalline orientations within grains are randomly generated from a Sobol sequence (e.g. [27]) in order to approach an isotropic polycrystal while optimizing the number of grains. The number of grains and voxels taken for the unit cell follows from the two parametric studies in order to determine the "optimal" configuration, with a good compromise between the computation time and the representativeness of the polycrystal. Simulations are performed on unirradiated specimens at a temperature of 25°C and a constant strain rate of $\dot{E} = 5\times10^{-4}s^{-1}$. The following parameters are considered, $\rho_{init}^{(s)} = 4.5\times10^{12}\ m^{-2}$, $d = 7.6\ \mu m$, $K_{auto} = 72$, $K_{forest} = 24$ and $p_y = 2.6\ nm$.

First, a convergence study for the spatial discretization is carried out. A polycrystal with 125 grains is considered. A total of seven spatial discretizations (in voxels per grain) are tested: 2^3, 4^3, 6^3, 8^3, 10^3, 12^3 and 14^3. For each discretization level, ten microgeometries for the Voronoi tesselation are generated. The stabilization of the macroscopic response is evaluated with respect to the highest resolution (considered as

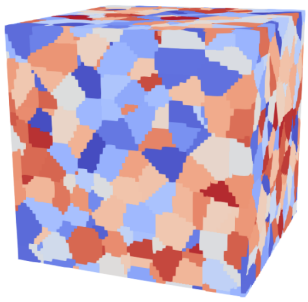

Figure 1: Unit cell with 729 grains and 373,248 voxels employed in the numerical simulations.

a reference and denoted hereafter k_{14^3}) by two relative errors, corresponding to the Hölder mean of order 1 and infinity, respectively. For defining these two errors a discretization of the time interval is considered, $0s = t_1 < t_2 < \ldots < t_N = 200s$ and the two relative errors are defined by

$$\delta_1 = \frac{1}{N}\sum_{p=1}^{N}\frac{|k_{14^3}(t_p) - k_\alpha(t_p)|}{|k_{14^3}(t_p)|} \qquad \text{and} \qquad \delta_\infty = \max_p\left\{\frac{|k_{14^3}(t_p) - k_\alpha(t_p)|}{|k_{14^3}(t_p)|}\right\}, \tag{15}$$

where the index α refers to the spatial discretization. Figure 2 displays the values of these two errors with respect to the ten microgeometries considered for each discretization. Through these results, it appears that a good compromise between size and precision is obtained for 8^3 or 512 voxels per grain. From this discretization, low values of the two relative errors are observed, as well as a low dispersion of results. This discretization is retained in what follows. Taking as reference the results for the highest resolution (14^3 voxels per grain) does not allow to characterize how close the results obtained for 512 voxels per grain are from the exact solution of the problem. A recent convergence result [28] shows that for linear heterogeneous materials the effective moduli obtained by the basic scheme converge to the theoretical effective moduli (as defined by the linear homogenization theory) when the resolution tends to infinity. To the best of our knowledge, there is no similar result for nonlinear materials, but it is reasonable to suppose that a higher resolution allows to better approximate the exact solution of the problem.

Second, the number of grains of the RVE plays a role in the macroscopic isotropy of the polycrystal. A study was carried out in order to characterize the isotropy of the polycrystal through its response to simple tensile type loadings in three different orthogonal directions. Nine numbers of grains in the RVE are considered: 2^3, 3^3, 4^3, 5^3, 6^3, 7^3, 8^3, 9^3 and 10^3 and for each, five microgeometries are used. As for the previous study, the mechanical response for each tensile direction is characterized by the stress level $k(t)$ versus time t. The deviation from the macroscopic isotropy is evaluated by two values, corresponding to the Hölder mean of order 1 and infinity and defined as

$$\Delta_1 = \frac{1}{N}\sum_{p=1}^{N}\frac{|k_{max}(t_p) - k_{min}(t_p)|}{|k_{avg}(t_p)|} \qquad \text{and} \qquad \Delta_\infty = \max_p\left\{\frac{|k_{max}(t_p) - k_{min}(t_p)|}{|k_{avg}(t_p)|}\right\}, \tag{16}$$

where $k_{max}(t_p) = \max\left\{k_{[100]}(t_p),\ k_{[010]}(t_p),\ k_{[001]}(t_p)\right\}$, $k_{min}(t_p) = \min\left\{k_{[100]}(t_p),\ k_{[010]}(t_p),\ k_{[001]}(t_p)\right\}$, and $k_{avg}(t_p) = \frac{1}{3}\left(k_{[100]}(t_p) + k_{[010]}(t_p) + k_{[001]}(t_p)\right)$. The subscript [100], [010] or [001] refers to the loading direction. Figure 3 displays the value of Δ_1 and Δ_∞ over the five microgeometries, for each number of grains. The isotropy of the polycrystal seems rather well respected from $9^3 = 729$ grains, with values of Δ_1 and Δ_∞ less than 1% and a low dispersion of results.

In conclusion, a satisfactory unit cell results with 729 grains, each of which is discretized by about 512 voxels. The cell is shown in Figure 1. With this cell, smooth convergence of the algorithm is observed.

4.2. Macroscopic response

A collection of uniaxial curves for specimens of steel type A under various conditions was generated with the homogenized model to infer the material parameters K_{auto}, K_{forest}, K_{SC} and p_y characterizing the evolution of the intragranular mean-free path of dislocations with deformation. Specifically, we consider unirradiated and irradiated specimens deforming at four different temperature levels ($-100°C$, $-60°C$, $25°C$ or $28°C$, $200°C$). Irradiated specimens were subject to intermediate (3.6×10^{23} $n.m^{-2}$) and high (7.5×10^{23} $n.m^{-2}$) fluences typical of RPV steels in pressurized water reactors. In all cases, the microstructural parameters $\rho_{init}^{(s)} = 4.5 \times 10^{12}$ m^{-2} and $d = 7.6$ μm are adopted. In the case of irradiated specimens, the irradiation parameters $d_{SC} = 3$ nm and $c_{SC} = 20.3/31.5 \times 10^{22}$ m^{-3} for the intermediate/high fluence are adopted. Several collections of curves were obtained by sweeping the material parameters K_{auto}, K_{forest}, K_{SC} and p_y across expected ranges of values. Figure 4 shows comparisons between the experimental curves of [1] and the predictions for a constant strain rate $\dot{E} = 5 \times 10^{-4} s^{-1}$ obtained with the parameters reported in Table 4. The main observation in the context of this figure is that good agreement is obtained for all twelve scenarios. Indeed, the homogenized model is seen to accurately reproduce both the elastic and viscoplastic regimes at all temperatures and irradiation conditions considered. By contrast, the model is seen to miss entirely the peak stress upon yielding observed in the experimental curves. In this connection, it is recalled that peak stresses in steels have been attributed to the unpinning of Cottrel atmospheres of dislocations, which is known as static ageing. Thus, values of peak stresses tend to be highly sensitive to the thermomechanical history of the specimen and therefore show strong variability. This is one of the reasons why engineering models usually omit their description. A second reason for omitting their description is that the subsequent softening can induce localized deformations and therefore result in mesh-dependent structural

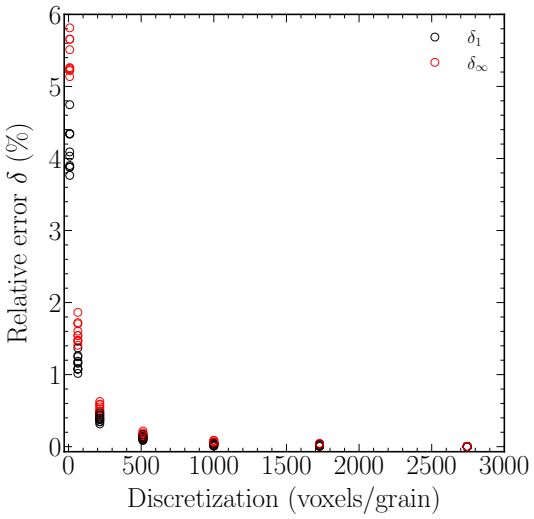

Figure 2: Relative errors with respect to the highest resolution versus voxels per grain

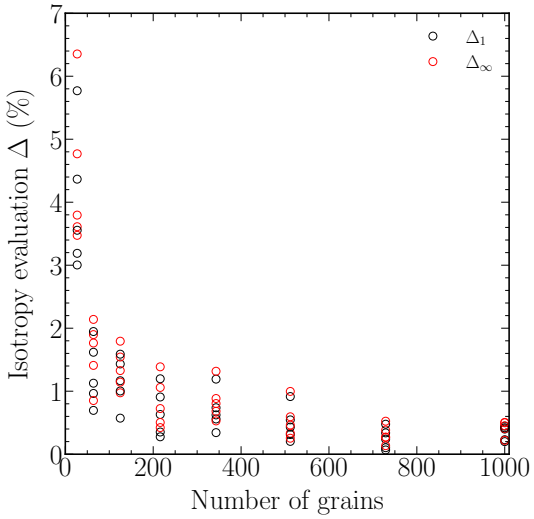

Figure 3: Quantitative estimates for the gap to the macroscopic isotropy versus the number of grains

	$\rho_{init}^{(s)}$ (m^{-2})	d (μm)	K_{auto}	K_{forest}	K_{SC}	p_y (nm)
A	4.5×10^{12}	7.6	72	24	30	2.6
B	3.5×10^{12}	5.25	72	24	30	2.6
C	3.7×10^{12}	7.6	72	24	30	2.6
D	4.5×10^{12}	7.6	72	24	30	2.6

Table 4: Parameters identified for the various types of steel considered in this study

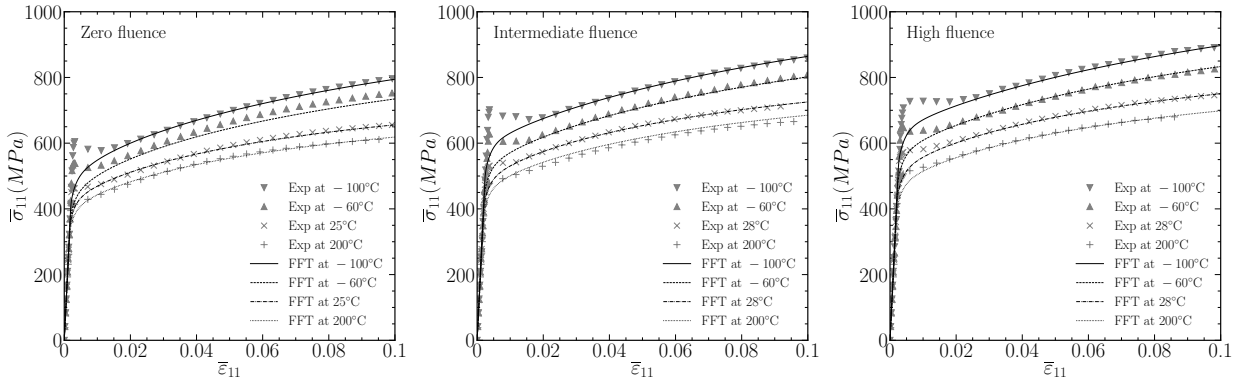

Figure 4: Comparison between experimental data and numerical simulations results of the macroscopic response of a polycrystal, under simple traction loading, for three levels of fluence : non-irradiated steel (left), intermediate fluence (center), high fluence (right)

simulations. Interestingly, recent multiscale simulations coupling the dynamics of irradiation defects and dislocation assembles at different spatial and temporal scales in steels suggest that, while present in the post-irradiated mechanical response, peak stresses may be absent from the mechanical response during irradiation [29]. In any event, the model can be employed to generate predictions for the evolution of a yield stress with temperature and strain rate by following common practice and defining the yield stress as the stress defined by the intercept between the tangent of the tensile curve at a deformation of 0.02 and the straight line representing the elastic part of the curve. Experimental values for a yield stress so defined in unirradiated steel specimens of type B at different strain rates have been reported in [30] (experimental values obtained from quasi-static tensile tests as well as dynamic tests using Hopkinson split bars). The values are plotted in Figure 5 versus temperature. Model predictions were generated with the parameters specified in Table 4 and imposed strain rates $\dot{E}_1 = 4.0{\times}10^{-4}\ s^{-1}$, $\dot{E}_2 = 17.6\ s^{-1}$ and $\dot{E}_3 = 4000\ s^{-1}$. A very good agreement between experimental and numerical results is observed for the low and moderate strain rates, and fair agreement is observed for the highest strain rate. Thus, the model successfully captures the nonlinear decrease of yield stress with temperature at the lower strain rates. Similarly, experimental results reported in [31] for steel specimens of type C can be employed to assess the capabilities of the model to describe the influence of irradiation on hardening. Corresponding simulations are performed with the material parameters of Table 4 at $T = 25°\text{C}$, $\dot{E} = 5{\times}10^{-4}\ s^{-1}$, and three different irradiation fluxes ($3{\times}10^{15}$, $8{\times}10^{15}$, $1{\times}10^{18}\ n.m^{-2}.s^{-1}$). To each flux correspond certain values of concentration and size of solute clusters. The values employed in the simulations are those experimental values reported in [31] and reproduced in Table 5. Experimental and simulated results for the magnitude $\Delta R_{p0.2} = \overline{\sigma}_{11}^{irr} - \overline{\sigma}_{11}^{unirr}\big|_{\overline{\varepsilon}_{11}^{vp}=0.002}$ are compared in Figure 6. An excellent correlation in all cases is observed. Finally, the concurrent influence of temperature and strain rate on the macroscopic response can be investigated by imposing sudden strain rate variations and measuring the induced stress jumps. Experimental measurements on steel specimens of type D have been reported in [32]. Corresponding simulations are generated with the material parameters of Table 4 by considering two pairs of strain rate variations ($5{\times}10^{-4}\ s^{-1} - 5{\times}10^{-3}\ s^{-1}$) and ($5{\times}10^{-5}\ s^{-1} - 5.0{\times}10^{-4}\ s^{-1}$), for five temperatures spanning the range $-100°\text{C}$ to $100°\text{C}$, and two fluences (non-irradiated and $10 \times 10^{23}\ n.m^{-2}$). This steel was subjected to irradiation in the Material Testing Reactor OSIRIS (CEA). Accelerating irradiation results from a flux which is approximately forty times higher than the flux seen by a RPV in a French pressurized water reactor [32]. At this irradiation levels the solute cluster size and concentration are $d_{SC} = 3\ nm$ and $c_{SC} = 35.1 \times 10^{22}\ m^{-3}$, respectively. The simulated macroscopic tensile curves are reported in Figures 7 and 8. Two series of jumps are performed for each pair of strain rates. At 2% of viscoplastic deformation, a positive strain rate jump is imposed and the strain rate value is maintained until 4% of viscoplastic deformation, followed by a negative strain rate jump, with the same amplitude. The same procedure is repeated between 6% and 8% of viscoplastic strain. In order to investigate the effect of the history of the strain rate on the macroscopic response, the low value of the pair ($5 \times 10^{-4}\ s^{-1} - 5 \times 10^{-3}\ s^{-1}$) and the

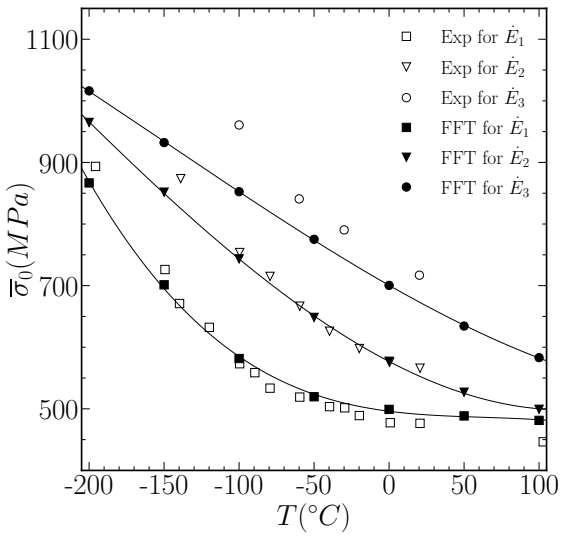

Figure 5: Evolution of the yield stress according to the temperature and the strain rate (each solid line corresponds to a quadratic fit of the FFT results)

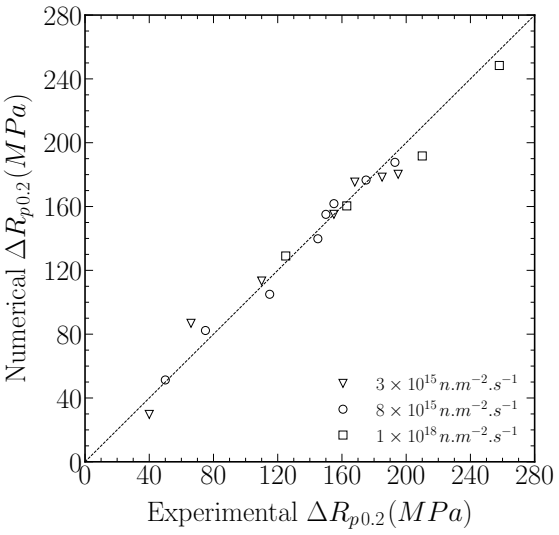

Figure 6: Comparison between experimental and numerical irradiation hardening for a total of 19 fluences through 3 fluxes

high value of the pair (5×10^{-5} s^{-1} – 5.0×10^{-4} s^{-1}) has been chosen equal. The simulated tensile curves reported in Figures 7 and 8 show that the behaviors of both unirradiated and irradiated specimens are almost insensitive to the strain rate history. Moreover, the strain-hardening rate (slope of the stress-strain curve) right after the jump is the same as the strain-hardening rate observed before the jump. The flow stress increases with strain rate, but the amplitude of the induced stress jumps decreases with temperature, to the extent that at $T = 100$°C, for the unirradiated material, the jump is about 0.2% of the flow stress, and for the irradiated material this ratio is almost twice. The stress jump, simply defined as an absolute difference of two stress values, is then recorded for each curve of Figures 7 and 8 and is compared with the experimental results of [32]. Figures 9 and 10 show the numerical and experimental stress jumps as a function of the temperature, according to the considered fluence. A good agreement is observed between the experimentally measured jumps and those predicted by the simulations, over the entire range of temperature considered, whether for the non-irradiated or the irradiated 16MND5 steel.

It is concluded that the model confected in this work with a simplified crystal plasticity law and a computational homogenization method based on Fast Fourier Transforms has the capability to accurately describe the response of irradiated bainitic steels under a wide range of temperatures, irradiation levels and strain rates.

4.3. Effects of the initial dislocation densities

In almost all simulations of crystalline agreggates reported in the litterature, the initial values of the material parameters (in our case the dislocation density and grain size) are taken identically for all integration points. However, several microstructure investigations have confirmed that dislocation distribution is quite heterogenious [33]. For the first time, to the knowledge of the authors, we study the influence of the heterogeneity of dislocation distribution of the local fields and macroscopic response in an unirradiated RPV steels. Numerical simulations are carried out considering a polycrystal composed of 216 grains and discretized by 125^3 voxels. This discretization value is adopted by a convergence study carried out on the average value per phase of the Von Mises equivalent viscoplastic strain, where different resolutions are considered from 25^3 to 250^3 voxels. The imposed loading corresponds to a simple traction in the direction [1, 0, 0] for a strain rate equal to 5×10^{-4} s^{-1} and for a temperature of 25°C. The following parameters are fixed in this study $\rho_{init}^{(s)} = 4.5 \times 10^{12}$ m^{-2}, $d = 7.6$ μm, $K_{auto} = 72$, $K_{forest} = 24$ and $p_y = 2.6$ nm. The convergence with respect to the resolution is evaluated by comparison with the highest considered resolution

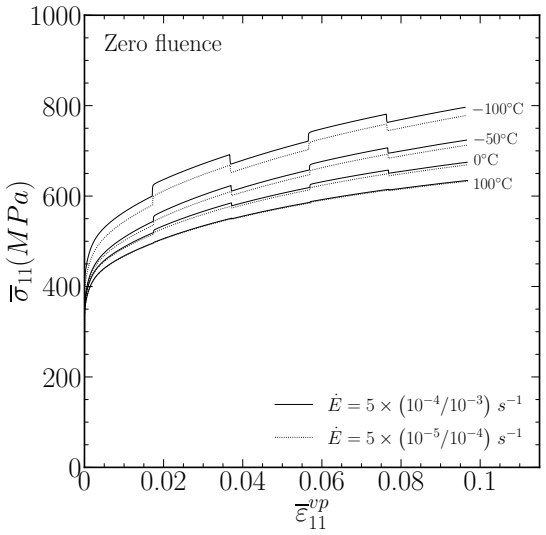

Figure 7: Simple tension behavior with abrupt strain rate variations for a non-irradiated 16MND5 steel

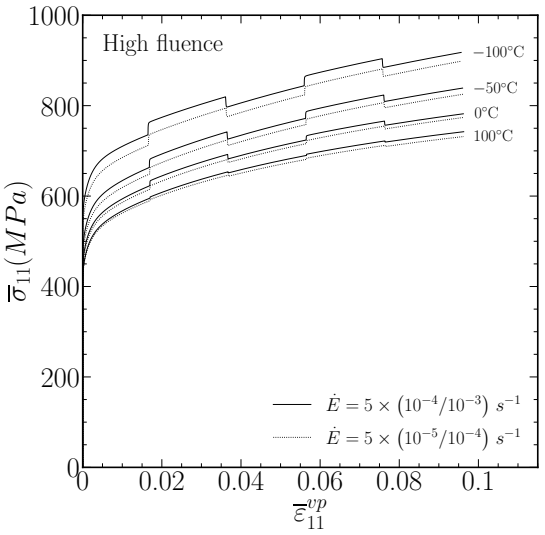

Figure 8: Simple traction behavior with abrupt strain rate variations for an irradiated 16MND5 steel

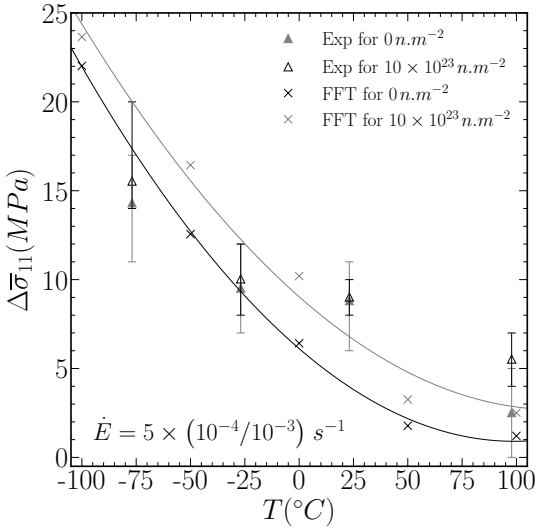

Figure 9: Stress jump as a function of the temperature for $5 \times 10^{-4}\ s^{-1}$ / $5 \times 10^{-3}\ s^{-1}$ strain rate variation (each solid line corresponds to a quadratic fit of the FFT results)

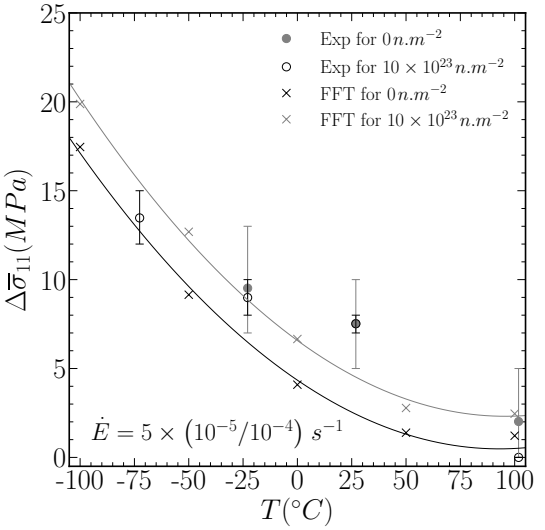

Figure 10: Stress jump as a function of the temperature for $5{\times}10^{-5}\ s^{-1}$ / $5{\times}10^{-4}\ s^{-1}$ strain rate variation (each solid line corresponds to a quadratic fit of the FFT results)

by a relative error δ, corresponding to the Hölder mean of order 1, as previously. The relative error in each phase is defined by

$$\delta = \frac{\left| \left(\overline{\varepsilon_{vp}^{eq}}^{(r)} \right)_{250} - \left(\overline{\varepsilon_{vp}^{eq}}^{(r)} \right)_{\alpha} \right|}{\left| \left(\overline{\varepsilon_{vp}^{eq}}^{(r)} \right)_{250} \right|} \tag{17}$$

where r refers to the phase, $\overline{\varepsilon_{vp}^{eq}}^{(r)}$ denotes the average value per phase of the Von Mises equivalent viscoplastic strain ε_{vp}^{eq} and α refers to the considered resolution. The results are presented in Figure 11 for a viscoplastic

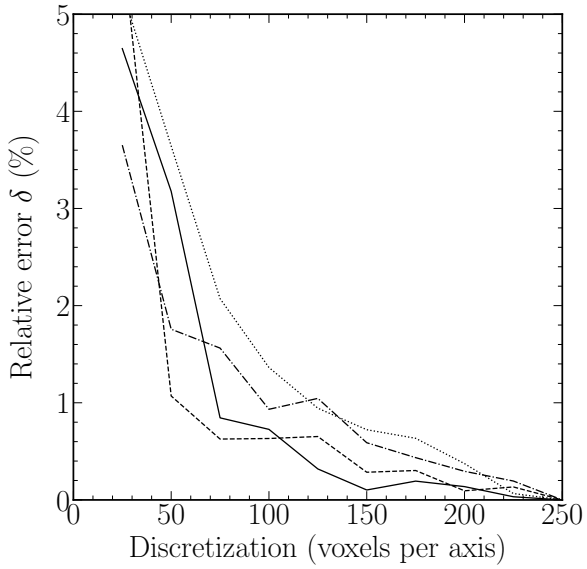

Figure 11: Relative errors with respect to the highest resolution versus total number of voxels

strain field obtained at 0.004 of total macroscopic strain in the tensile direction and for 4 different phases corresponding to the slowest convergence. Finally, a discretization of 125^3 voxels is chosen, corresponding to a relative error δ less than 1% and allowing then a good compromise between precision and calculation time.

In this study, the initial dislocation densities consists in a field defined over the polycristal domain. Three distributions of the initial dislocation densities are considered:

1. an uniform distribution, where the initial dislocation densities are constant (equal to $\rho_{init}^{(s)}$) in the whole polycrystal,
2. a homogeneous per phase distribution, where the initial dislocation densities are uniform in each phase,

flux $(n.m^{-2}.s^{-1})$	d_{SC} (nm)	c_{SC} $(10^{22}\ m^{-3})$	exp hard (MPa)	flux $(n.m^{-2}.s^{-1})$	d_{SC} (nm)	c_{SC} $(10^{22}\ m^{-3})$	exp hard (MPa)
8×10^{15}	2.0	16.72	50.0	3×10^{15}	2.5	25.68	110.0
8×10^{15}	2.4	19.35	75.0	3×10^{15}	2.7	32.04	155.0
8×10^{15}	2.6	21.74	115.0	3×10^{15}	2.85	33.43	168.0
8×10^{15}	2.6	30.44	145.0	3×10^{15}	3.1	28.86	185.0
8×10^{15}	2.7	32.04	150.0	3×10^{15}	3.2	27.41	195.0
8×10^{15}	2.8	31.34	155.0	1×10^{18}	2.15	40.38	125.0
8×10^{15}	2.86	33.49	175.0	1×10^{18}	2.2	50.25	163.0
8×10^{15}	3.1	30.79	193.0	1×10^{18}	2.2	62.81	210.0
3×10^{15}	2.0	9.55	40.0	1×10^{18}	2.2	87.93	258.0
3×10^{15}	2.1	26.82	66.0				

Table 5: Experimental hardening according to the size and concentration of solute clusters

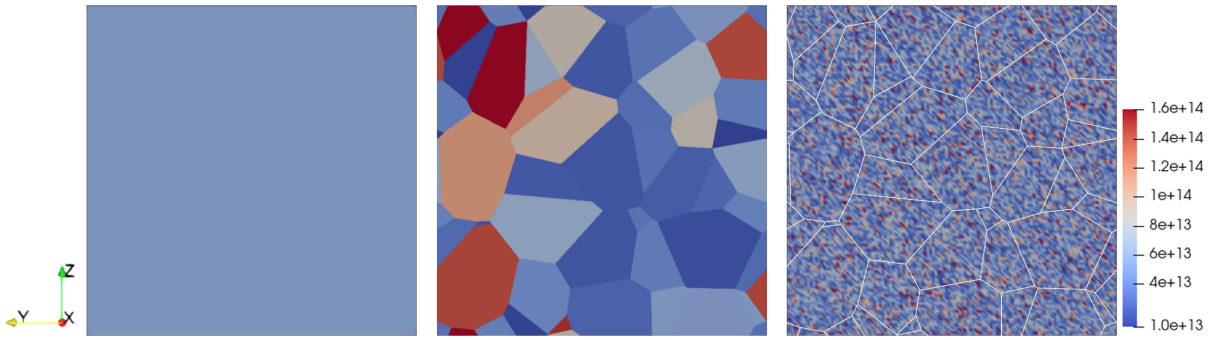

Figure 12: Initial dislocation densities fields: homogeneous (left), homogeneous per phase (center) and heterogeneous (right)

but different from one phase to another,

3. a heterogeneous distribution, where each voxel has a different initial dislocation density, regardless of the phase in which it is located.

Except for the case of a uniform distribution, the value of the initial dislocation density is a random variable and, in order to be able to compare the results obtained for these three distributions, its mean is the same for the three distributions and equal to $\mu_{init} = \rho_{init}^{(s)}$. Moreover, the standard deviation of this random variable is fixed to $\sigma_{init} = 5\mu_{init}$. The values of the initial dislocation densities are randomly drawn according to a probability distribution law (18) and (19) of the log-normal type. The choice of this law was determined by three requirements dictated by physical requirements: drawn values should be positive, the maximum value of initial dislocation densities should be close to the average value $\rho_{init}^{(s)}$ and the range of values between the maximal one and its half should be large enough.

The probability density for a log-normal law is given by

$$p(x,\ \mu_{log},\ \sigma_{log}) = \frac{1}{x\sigma_{log}\sqrt{2\pi}}\ \exp\left(-\frac{(\ln(x)-\mu_{log})^2}{2\sigma_{log}^2}\right), \tag{18}$$

where the parameters μ_{log} and σ_{log} are related to the mean μ_{init} and standard deviation σ_{init} by

$$\mu_{log} = \ln(\mu_{init}) - \frac{1}{2}\ln\left(\frac{\sigma_{init}^2}{\mu_{init}^2}+1\right) \quad \text{and} \quad \sigma_{log} = \sqrt{\ln\left(\frac{\sigma_{init}^2}{\mu_{init}^2}+1\right)}. \tag{19}$$

The values of the initial dislocation densities are obtained using a random variable with uniform distribution. The three initial dislocation densities fields obtained by this procedure are presented in Figure 12 for a specific cross section.

The macroscopic response and the evolution of the total dislocation density obtained for each distribution of the initial dislocation densities are presented in Figure 13 for three temperatures, -100°C, 25°C and 200°C, considering the same parameters than previously. The total dislocation density is defined as

$$\overline{\rho} = \sum_{r=1}^{216}\sum_{s=1}^{12} c^{(r)}\overline{\rho}^{(r,s)} \tag{20}$$

where $c^{(r)}$ represents the volume fraction of the phase r. The initial value of $\overline{\rho}$ is denoted by $\overline{\rho}_{init}$. For the macroscopic response, very small differences are observed between the three distribution configurations over the strain range studied and for the three temperatures considered. At -100°C, the macroscopic responses are superposed, while at 25°C and 200°C, small differences are observed at the beginning of the viscoplastic domain between the homogeneous distribution and the two others. Nevertheless these differences tend to

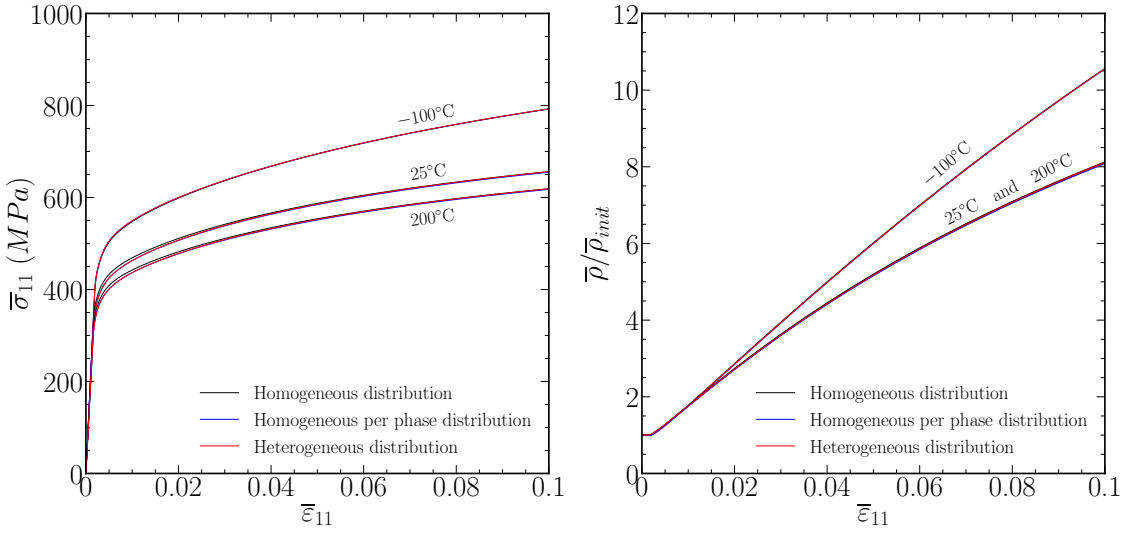

Figure 13: Macroscopic response (a) and total dislocation density, normalized by its initial value (b), for three distributions of the initial dislocation densities and for three temperatures, -100°C, 25°C and 200°C

reduce as the macroscopic strain increase. Concerning the evolution of the total dislocation density, it seams that the distribution of the initial dislocation densities has almost no effect on this macroscopic variable. The results for 25°C and 200°C are superimposed and this is probably due to the fact that the annihilation distance y as given by (10) no longer depends on the temperature if this one is greater than 25°C. The temperature level has a notable effect on the evolution of the total dislocation density with respect to the macroscopic strain; at low temperatures (-100°C) this evolution is less non linear and more rapidly increasing than at high temperatures (25°C and 200°C). This could be explained by the increasing of the annihilation distance (10) with the temperature which leads a diminution of the dislocation densities rates (8).

The effects of the initial dislocation densities are observed by analysing the Von Mises equivalent viscoplastic strain and the maximum principal stress value, which are respectively defined by

$$\varepsilon_{vp}^{eq} = \sqrt{\frac{2}{3}\,\boldsymbol{\varepsilon}_{vp}^{d} : \boldsymbol{\varepsilon}_{vp}^{d}}, \qquad \text{and} \qquad \sigma_{p}^{max} = \max\left(\sigma_1,\ \sigma_2,\ \sigma_3\right), \tag{21}$$

where $\boldsymbol{\varepsilon}_{vp}^{d}$ represents the deviatoric part of the viscoplastic strain tensor and σ_i, $i = 1, 2, 3$ are the principal stresses. The local fields retained for this analysis are obtained for two effective strain values in the loading direction: $\overline{\varepsilon}_{11} = 0.004$ (which corresponds to $\overline{\varepsilon}_{vp_{11}} = 0.002$, *i.e.* the value considered for the determination of the conventional yield stress) and $\overline{\varepsilon}_{11} = 0.1$. The first value of the macroscopic strain corresponds to the situation where the macroscopic response (Figure 13) presents the most significant difference between the three distributions considered, whereas for the second value this difference is completely smeared out.

Figure 14 presents the equivalent viscoplastic strain fields obtained for a uniform distribution, at $\overline{\varepsilon}_{11} = 0.004$ for three resolutions, 57^3, 125^3 and 250^3 voxels. Deformation bands can be seen in the grains circled in red, but this aspect is theoretically impossible for the case of a homogeneous distribution because the considered crystal plasticity law is not supposed to induce localizations. Furthermore, the width and number of bands evolve with the resolution, which means that this problem clearly corresponds to an artifact of the FFT method. In fact, it is here the non-respect of the grain boundaries geometry (seen as staircases) which favours the appearance of non-physical deformation bands. The work of [34] focuses on this problem and shows that the appearance of strain bands is greatly reduced by using a non regular Fourier grid, in order to correctly match the grain boundaries geometry. This aspect is therefore a prospect of this work. However, in the analysis presented hereafter the values of the local filds have no particular meaning, the analysis being purely qualitative.

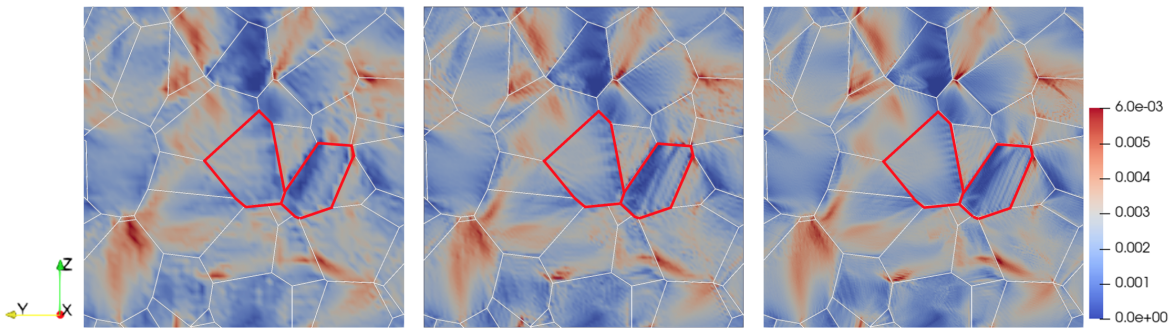

Figure 14: Von Mises equivalent viscoplastic strain fields (homogeneous distribution at $\overline{\varepsilon}_{11} = 0.004$) for three resolutions: 57^3 (left), 125^3 (center) and 250^3 (right) voxels

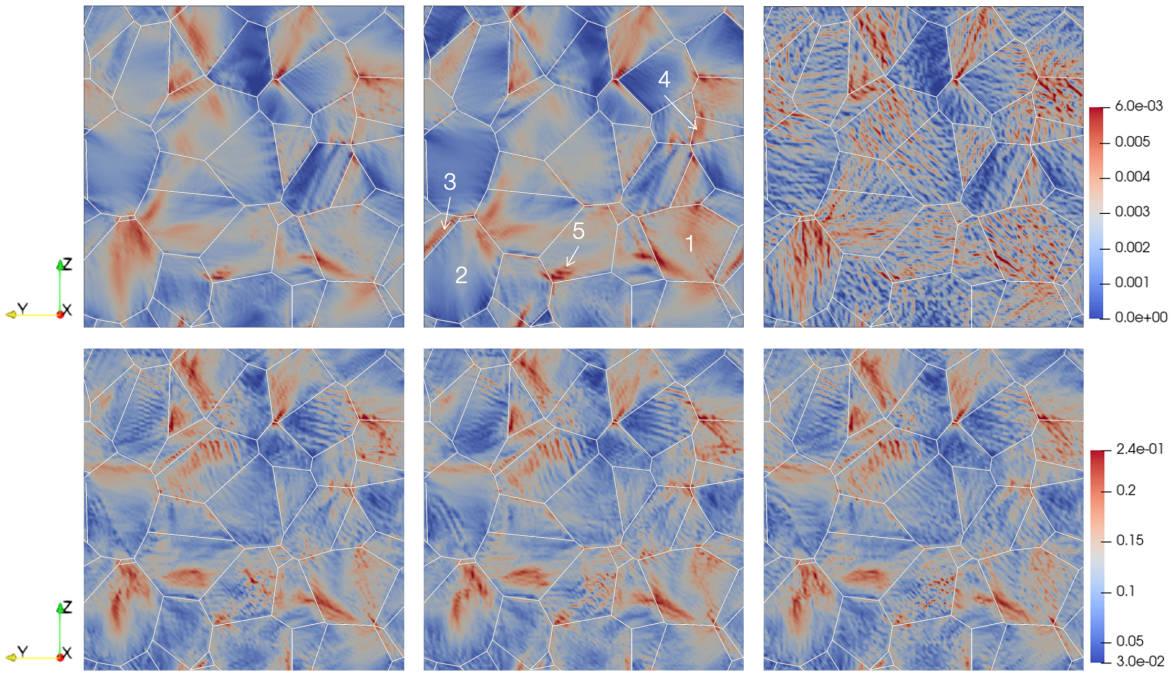

Figure 15: Von Mises equivalent viscoplastic strain fields: at $\overline{\varepsilon}_{11} = 0.004$ (up) and $\overline{\varepsilon}_{11} = 0.1$ (down)

Figures 15 and 16 present respectively the Von Mises equivalent viscoplastic strain field and the maximum principal stress field, for the three distributions: homogeneous (left), homogeneous per phase (center) and heterogeneous (right). At $\overline{\varepsilon}_{11} = 0.004$, three distinct field profiles are clearly identified, both for the equivalent viscoplastic strain and for the maximum principal stress value. Comparing the equivalent viscoplastic strain maps, between the homogeneous and homogeneous per phase distributions a strong correlation is observed between the level of the initial dislocation densities of the grains and the overall viscoplastic strain of the grains. For instance, for the grains denoted (1) and (2) on the Figure 15 the initial dislocation density is lower (for grain (1)) or higher (for grain (2)) than the mean value (affected to all grains in the case of an homogeneous distribution) and the overall viscoplastic strain is higher in grain (1) or lower in the grain (2) than the corresponding values obtained for the same grains in the case of an homogeneous distribution. Also, in the case of the homogeneous per phase distribution, notable strain localization are observed at the grain boundaries (3), (4) or at triple points (5). When comparing the maps corresponding to the homogeneous and heterogeneous distributions, the main differences are observed for the fields profiles, inside each grain,

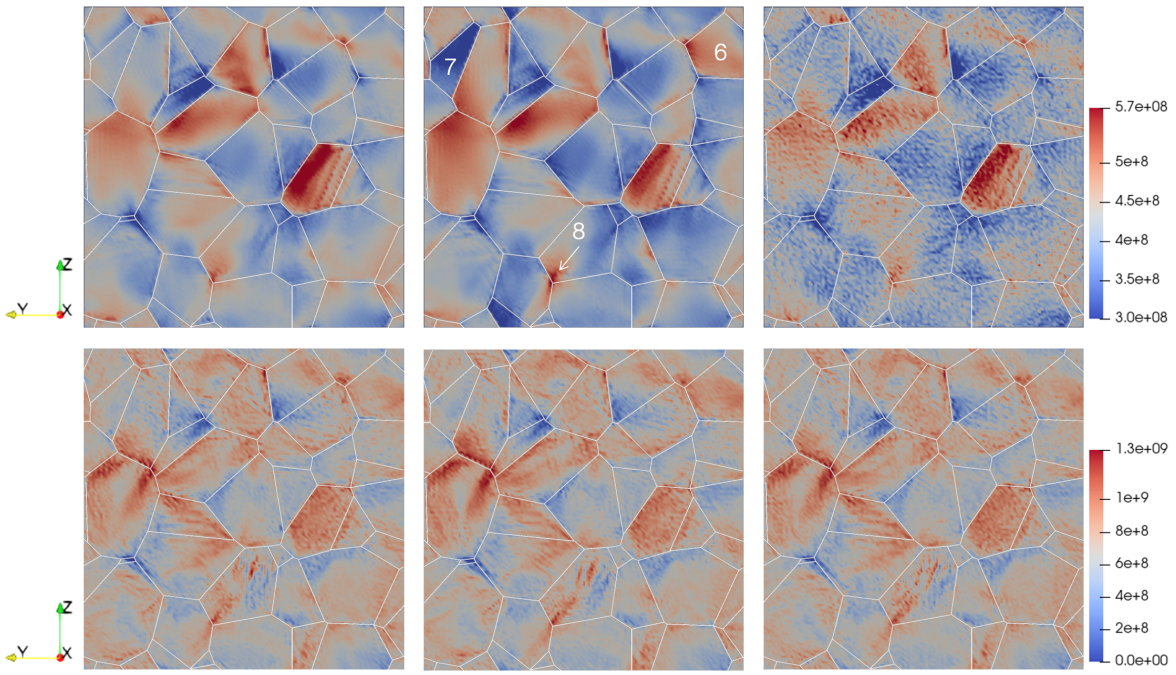

Figure 16: Maximum principal stress value fields: at $\overline{\varepsilon}_{11} = 0.004$ (up) and $\overline{\varepsilon}_{11} = 0.1$ (down)

due to the significant difference in initial dislocation densities from one voxel to the other nearby ones for the heterogeneous distribution. Similar conclusions can be drawn for the maximum principal stress value. The major differences between homogeneous and heterogeneous distributions are observed in the field profiles within each grain. In contrast, between homogeneous and homogeneous per phase distributions, higher (6) or lower (7) overall grain viscoplastic strain can be observed, similarly for stress concentrations (8).

Deep in the plastic range the observed differences between the local fields corresponding to different initial dislocation densities distributions tend to gradually fade away as the loading evolves during the simulation, to finally converge towards a common configuration. In particular, at $\overline{\varepsilon}_{11} = 0.1$, the local fields present similar profiles for the two results of interest, whatever the type of initial dislocation densities distribution considered.

As explained in the previous section, the local values of the fields could be not very accurate, but as shown on the Figure 11 the average value per phase of the Von Mises equivalent viscoplastic strain has an asymptotic behavior when the resolution increases. Therefore it is pertinent to compare these mean values for the three types of the initial dislocation densities distributions. The results are reported in Figure 17. In these figures, we select the first 50 phases which present the maximum difference value observed between the three distributions at $\overline{\varepsilon}_{11} = 0.004$ and the average values per phase are ordered (on the x-axis) in a decreasing manner with respect to this difference value. These results show, as previously, that the impact of the distribution of initial dislocation densities for a low strain ($\overline{\varepsilon}_{11} = 0.004$) is more prononced than for a high strain ($\overline{\varepsilon}_{11} = 0.1$). Furthermore, these results also highlight that the homogeneous and heterogeneous distributions give very closed values for the average value per phase compared to analogous result for the homogeneous per phase distribution. This could be the consequence of a statistical effect. Each grain contains sufficiently voxels such way that the mean value of the initial dislocation density in each grain is close to the mean value of the same variable on the whole domain, so close to the value of the uniform distribution.

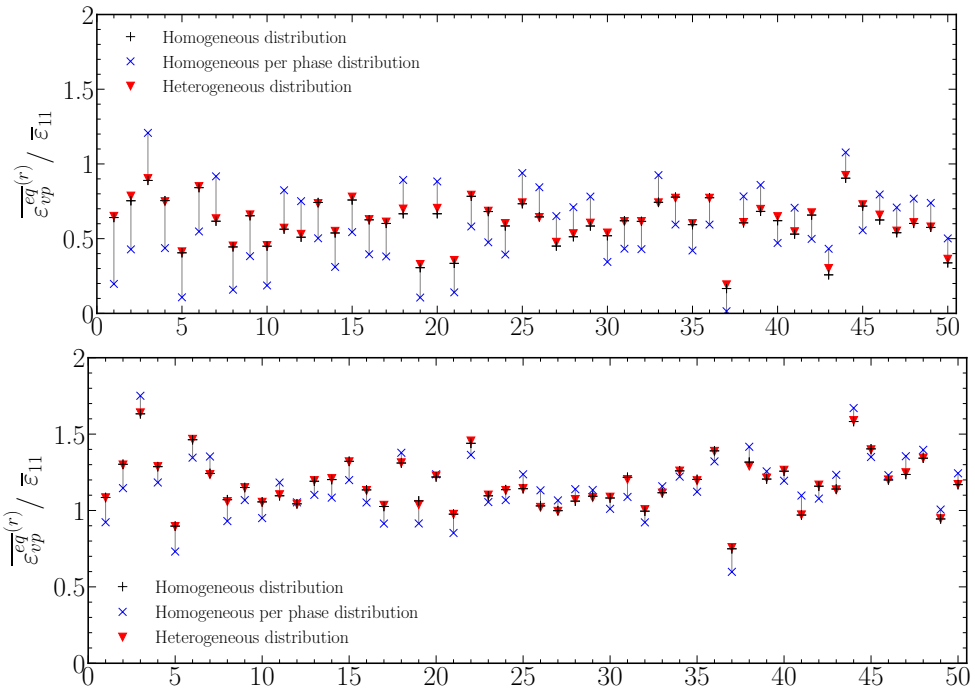

Figure 17: Average value per phase of the Von Mises equivalent viscoplastic strain: at $\bar{\varepsilon}_{11} = 0.004$ (up) and $\bar{\varepsilon}_{11} = 0.1$ (down)

5. Conclusion

A multi-scale model has been proposed by combining a crystal plasticity law for irradiated RPV steels and numerical full-field simulations on polycrystals based on Fast Fourier Transforms. Comparisons between numerical and experimental results have been performed on four types of macroscopic results in order to show the relevance of the crystal plasticity law. First, the macroscopic tensile curves are accurately reproduced by the numerical simulations, for a temperature range from -100°C to 200°C and for three fluences. Second, the strain rate sensitivity induced by a fast variation in imposed macroscopic strain rate shows a good agreement with the experimental results for a temperature range from -200°C to 100°C and for two strain-rate variations $5 \times 10^{-3}\ s^{-1}$ / $5 \times 10^{-4}\ s^{-1}$ and $5 \times 10^{-4}\ s^{-1}$ / $5 \times 10^{-5}\ s^{-1}$. Third, the evolution of the yield stress is generally better reproduced for low and high strain rates ($4 \times 10^{-4}\ s^{-1}$ and $17.6\ s^{-1}$) than for a very high strain rate ($4000\ s^{-1}$). Finally, the irradiation-induced hardening is well reproduced by numerical simulations, over a wide range of fluences and fluxes. In these simulations, all input parameters are within typical values of grain size, dislocation densities and solute cluster size and density, characteristic of a irradiated low alloy RPV steels. The main advantage of this physically-based model is that when the yield stresses before and after irradiation are known at a given temperature and strain rate, the model can predict the yield stress at any temperature and strain rate. In addition, intragranular stress and strain fields are also investigated in the case of heterogeneous distribution of initial dislocation densities. The results led to differences in local fields between the three distributions at the beginning of the viscoplastic domain, which tend to reduce and basically converge towards a common configuration deep in the viscoplastic domain. However, the presence of non-physical strain bands are observed representing an artifact of the FFT method and more precisely concerning the discretization process which not respect the grain boundaries geometry. Finally, the macroscopic response and the evolution of the total dislocation density seem to be very weakly influenced by the heterogeneity of dislocation density.

Acknowledgments

The work was funded by the Institute of Fusion and Instrumentation Sciences in Nuclear Environments (ISFIN) and by the Institut de Radioprotection et de Sûreté Nucléaire (IRSN). Additional funds from the Universidad Nacional de La Plata (UNLP) were received by M.I.I. through grant I281/2024. The authors gratefully acknowledge Hervé Moulinec for his assistance in using CraFT and useful discussions about FFT methods.

Data availability

This study has no part providing observations or experimentation data. All experimental results used in order to validate research findings presented in this article are public data, available from cited research publications and owned by their respective authors.

References

[1] G. Monnet, Analytical flow equation for irradiated low-alloy steels established by multiscale modeling, Journal of Nuclear Materials 586 (2023) 154647.
[2] J.-P. Mathieu, Analyse et modélisation micromécanique du comportement et de la rupture fragile de l'acier 16MND5: prise en compte des hétérogénéités microstructurales, Ph.D. thesis (2006).
[3] E. Bouyne, H. Flower, T. Lindley, A. Pineau, Use of EBSD technique to examine microstructure and cracking in a bainitic steel, Scripta Materialia (1998) 295–300.
[4] G. Monnet, L. Vincent, L. Gélébart, Multiscale modeling of crystal plasticity in reactor pressure vessel steels: Prediction of irradiation hardening, Journal of Nuclear Materials 514 (2019) 128–138.
[5] G. Monnet, L. Vincent, B. Devincre, Dislocation-dynamics based crystal plasticity law for the low- and high-temperature deformation regimes of bcc crystal, Acta Materialia 61 (16) (2013) 6178–6190.
[6] L. Chaix, M. Gărăjeu, P.-G. Vincent, G. Monnet, M. I. Idiart, Homogenized descriptions for the elastoplastic response of polycrystalline solids with complex hardening laws: Application to neutron-irradiated bainitic steels, European Journal of Mechanics - A/Solids 105 (2024) 105258.
[7] H. Moulinec, P. Suquet, A fast numerical method for computing the linear and nonlinear properties of composites, C. R. Acad. Sc. Paris II 318 (1994) 1417–1423.
[8] M. Schneider, A review of nonlinear FFT-based computational homogenization methods, Acta Mech 232 (2021) 2051–2100.
[9] A. Prakash, R. Lebensohn, Simulation of micromechanical behavior of polycrystals: Finite elements versus fast Fourier transforms, Modelling Simul. Mater. Sci. Eng (2009) 64010–16.
[10] S. El Shawish, P.-G. Vincent, H. Moulinec, L. Cizelj, L. Gélébart, Full-field polycrystal plasticity simulations of neutron-irradiated austenitic stainless steel: A comparison between FE and FFT-based approaches, Journal of Nuclear Materials 529 (2020) 151927.
[11] R. Lebensohn, N-site modeling of a 3d viscoplastic polycrystal using Fast Fourier Transform, Acta Materialia 49 (2001) 2723–2737.
[12] J. Segurado, R. Lebensohn, J. Llorca, Computational homogenization of polycrystals, Adv. Appl. Mech. 51 (2018) 1–114.
[13] J. Michel, H. Moulinec, P. Suquet, A computational method based on augmented lagrangians and Fast Fourier Transforms for composites with high contrast, Computer Modeling in Engineering & Sciences 1 (2) (2000) 79–88.
[14] D. Eyre, G. Milton, A fast numerical scheme for computing the response of composites using grid refinement, The European Physical Journal Applied Physics 6 (1999) 41–47.
[15] V. Monchiet, G. Bonnet, A polarization-based FFT iterative scheme for computing the effective properties of elastic composites with arbitrary contrast, Int. J. Numer. Meth. Engng 89 (2012) 1419–1436.
[16] H. Moulinec, F. Silva, Comparison of three accelerated FFT-based schemes for computing the mechanical response of composite materials, International Journal for Numerical Methods in Engineering 97 (13) (2014) 960–985.
[17] A. M. P. Brozzo, G. Buzzichelli, M. Mirabile, Microstructure and cleavage resistance of low-carbon bainitic steels, Metal Science 11 (1977) 123–130.
[18] F. Kocks, H. Mecking, Physics and phenomenology of strain hardening: The fcc case, Progress in Materials Science 48 (2003) 171–273. doi:10.1016/S0079-6425(02)00003-8.
[19] CRAFT, **C**omposite **R**esponse and **F**ourier **T**ransforms (free software).
URL `https://lma-software-craft.cnrs.fr`
[20] P. Suquet, A simplified method for the prediction of homogenized elastic properties of composites with a periodic structure, C. R. Acad. Sc. Paris, II 311 (1990) 769–774.
[21] H. Moulinec, P. Suquet, A numerical method for computing the overall response of nonlinear composites with complex microstructure, Computer Methods in Applied Mechanics and Engineering 157 (1) (1998) 69–94.
[22] L. Joëssel, P.-G. Vincent, M. Gărăjeu, M. I. Idiart, Viscoplasticity of voided cubic crystals under hydrostatic loading, International Journal of Solids and Structures 147 (2018) 156 – 165.

[23] P.-G. Vincent, H. Moulinec, L. Joëssel, M. I. Idiart, M. Gărăjeu, Porous polycrystal plasticity modeling of neutron-irradiated austenitic stainless steels, Journal of Nuclear Materials 542 (2020) 152463.
[24] C. Bellis, P. Suquet, Geometric variational principles for computational homogenization, Journal of Elasticity 137 (2019) 119–149.
[25] K. Wojtacki, P.-G. Vincent, P. Suquet, H. Moulinec, G. Boittin, A micromechanical model for the secondary creep of elasto-viscoplastic porous materials with two rate-sensitivity exponents: Application to a mixed oxide fuel, International Journal of Solids and Structures 184 (2020) 99–113.
[26] G. Boittin, P.-G. Vincent, H. Moulinec, M. Gărăjeu, Numerical simulations and modeling of the effective plastic flow surface of a biporous material with pressurized intergranular voids, Computer Methods in Applied Mechanics and Engineering 323 (2017) 174–201.
[27] R. Lebensohn, M. Idiart, P. Ponte Castañeda, P.-G. Vincent, Dilatational viscoplasticity of polycrystalline solids with intergranular cavities, Phil. Mag. 91 (2011) 3038–3067.
[28] Y. Changqing, E. T. Chung, Convergence of trigonometric and finite-difference discretization schemes for FFT-based computational micromechanics, BIT Numerical Mathematics 63 (1) (2023) 11.
[29] C. Ji, Y. Cui, Y. Li, N. Ghoniem, A concurrent irradiation-mechanics multiscale coupling model, Journal of the Mechanics and Physics of Solids 167 (2022) 105005.
[30] B. Tanguy, J. Besson, R. Piques, A. Pineau, Ductile to brittle transition of an a508 steel characterized by Charpy impact test: Part i: experimental results, Engineering Fracture Mechanics 72 (1) (2005) 49–72.
[31] P. B. Wells, T. Yamamoto, B. Miller, T. Milot, J. Cole, Y. Wu, G. R. Odette, Evolution of manganese–nickel–silicon-dominated phases in highly irradiated reactor pressure vessel steels, Acta Materialia 80 (2014) 205–219.
[32] J. Hure, C. Vaille, P. Wident, D. Moinereau, C. Landron, S. Chapuliot, C. Benhamou, B. Tanguy, Warm prestress effect on highly irradiated reactor pressure vessel steel, Journal of Nuclear Materials 464 (2015) 281–293.
[33] C. Robertson, K. Obrtlik, B. Marini, Dislocation structures in 16mnd5 pressure vessel steel strained in uniaxial tension at different temperatures from −196°c up to 25°c, Journal of Nuclear Materials 366 (2007) 58–69.
[34] M. Zecevic, R. Lebensohn, Recent advances in fft-based methods for polycrystalline materials, 2024.